



1
2
3 An Improved BRDF Hotspot Model and its Use in VLIDORT to Study the Impact
4 of Atmospheric Scattering on Hotspot Directional Signatures in the Atmosphere

5
6 Xiaozhen Xiong^{1*}, Xu Liu¹, Robert Spurr²,
7 Ming Zhao^{1,3}, Qiguang Yang^{1,3}, Wan Wu¹, Liqiao Lei^{1,3}
8

9 ¹ NASA Langley Research Center, Hampton, VA, USA

10 ² RT SOLUTIONS Inc., Cambridge, MA, USA

11 ³ Adnet Systems Inc., Bethesda, MD 20817, USA

12
13 Corresponding to: Xiaozhen Xiong (Xiaozhen.Xiong@nasa.gov)
14

15
16 **Abstract**
17

18 The term “hotspot” refers to the sharp increase of reflectance occurring when incident (solar) and
19 reflected (viewing) directions coincide in the backscatter direction. The accurate simulation of
20 hotspot directional signatures is important for many remote sensing applications. The RossThick-
21 LiSparse-Reciprocal (RTLSR) Bidirectional Reflectance Distribution Function (BRDF) model is
22 widely used in radiative transfer simulations, but it typically requires large values of numerical
23 quadrature and Fourier expansion terms in order to represent the hotspot accurately. In this paper,
24 we have developed an improved hotspot BRDF model that converges much faster, making it more
25 practical for use in atmospheric radiative transfer simulations of top-of-atmosphere (TOA) hotspot
26 signatures. Using the VLIDORT RT model, we found that reasonable TOA hotspot accuracy can
27 be obtained with just 23 Fourier terms for clear atmospheres, and 63 Fourier terms for atmospheres
28 with aerosol scattering.
29

30 We carried out a number of hotspot signature simulations with VLIDORT to study to the impact
31 of molecular and aerosol scattering on hotspot signatures. We confirmed that (1) atmospheric
32 scattering tends to smooth out the hotspot signature at the TOA, but has no impact on hotspot
33 width; and (2) the hotspot signature at the TOA in the near-infrared is larger than in the visible,
34 and has an obvious increase with the solar zenith angle. As the hotspot amplitude at the TOA with
35 aerosol scattering included is smaller than that with molecular scattering only, the amplitude of
36 hotspot signature at the surface is likely underestimated in the previous analysis based on the
37 POLDER measurements, where the atmospheric correction was based on a single-scatter
38 Rayleigh-only calculation. We also draw attenuation to a scaling factor of $3\pi/4$ which has been
39 applied to the Ross-Thick kernel with hotspot correction.
40

41
42 **Keywords:** BRDF, Hot Spot, VLIDORT, RTLSR
43
44
45



46
47
48

1. Introduction

49 Most land surfaces reflect incident light anisotropically. For a given incident sun angle, the surface
50 reflectance may vary by a factor of two in the near infrared [Kriebel et al., 1978]. An accurate
51 accounting of the anisotropic reflectance at the Earth's surface is very important for many remote
52 sensing applications, including monitoring of climate changes, mapping land covers, analyzing
53 vegetation densities, or inter-calibration between different satellite instruments (e.g. [Yang et al.,
54 2020] and references therein). Lorente et al. [2018] investigated the importance of surface
55 reflectance anisotropy with regard to cloud and NO₂ retrievals from satellite measurements by the
56 Global Ozone Monitoring Experiment 2 (GOME-2) and the Ozone Monitoring Instrument (OMI).
57 This study showed that retrieved cloud fractions have an east–west across-track bias of 10-50 %,
58 and under moderately polluted NO₂ scenarios with backward scattering geometry, clear-sky air
59 mass factors can be as much as 20% higher when surface anisotropic reflection is included in the
60 calculations.

61 The angular distribution of reflected light by a surface is normally represented mathematically by
62 the Bidirectional Reflectance Distribution Function (BRDF) [Nicodemus et al., 1992], which is a
63 function of the incident solar zenith angle, the reflected viewing zenith angle, and the relative
64 azimuth angle between these two directions. Usually, there is a strong increase in BRDF toward
65 the backscatter direction, with much smaller BRDF variations seen around the forward-scatter
66 direction. Peak BRDF values occur when backscatter incident and reflected directions coincide;
67 this sharp reflectance increase is usually referred to as the “hotspot” [Kuusk, 1985; Hapke, 1986].
68 The “hotspot” effect has been observed for a variety of planetary bodies, including the Moon,
69 Mars, asteroids, planetary satellites, as well as terrestrial vegetation [Bréon et al., 2002]. The most
70 widely accepted explanation for the hotspot effect is the so-called “shadow hiding” effect. Here,
71 particles at the surface (e.g. leaves, soil grains) cast shadows on adjacent particles; these shadows
72 are visible at large phase angles but at zero phase angle the shadows are hidden by the particles
73 that cast them. Coherent backscatter is another physical explanation of reflectance enhancement
74 in the hotspot direction [Kuga and Ishimaru, 1984; Hapke et al., 1993].

75 The bidirectional reflective spectra of land surfaces have been measured in laboratories, fields and
76 airborne experiments, or derived from satellite observations. The two most widely used
77 hyperspectral bidirectional reflective spectra of land surfaces are (1) the U.S. Geological Survey
78 (USGS) Spectral Library (Version 7) [Kokaly et al., 2017], comprising a very diverse land surface
79 BRDF data based with about 40,000 spectra in all, and (2) the ASTER Spectral Library from
80 NASA's Jet Propulsion Laboratory, with a collection of over 2,000 measured spectra [Baldridge
81 et al., 2009]. Using these two databases and RTLSR model, Yang et al. [2020] went on to develop
82 a Hyper-Spectral Bidirectional Reflectance (HSBR) model for remote sensing applications. BRDF
83 data derived from satellite observations have been used to evaluate and correct for anisotropy in
84 several instruments, including, for example, the Advanced Very High Resolution Radiometer
85 (AVHRR) [e.g. Gutman, 1987; Roujean et al., 1992], the Along-Track Scanning Radiometer
86 (ATSR-2) located on board the ERS-2 platform [Godsalve, 1995], and the MODerate resolution
87 Imaging Spectrometer (MODIS) [Wanner et al., 1997; Lucht et al., 2000; Schaaf et al., 2002].
88 However, the AVHRR, ATSR and MODIS instruments have limited viewing geometry options;
89 in contrast, the POLarization and Directionality of Earth Reflectances (POLDER) instrument on
90 board the Advanced Earth Observing Satellite (ADEOS) in August 1996 provided a much better



91 directional sampling to measure the BRDF up to 65° VZA (viewing zenith angle) and for the full
92 azimuth range [Deschamps et al., 1994]. So, these POLDER reflectance measurements were used
93 to examine the hotspot signature for different vegetated surfaces [Bréon et al., 2002].

94 Many BRDF models have been developed in order to simulate or reproduce directional signatures
95 of land surface reflectance. These include empirical models [Walthall et al., 1985], semi-empirical
96 models [Hapke, 1981, 1986; Rahman et al., 1993; Roujean et al., 1992; Wanner et al., 1995; 1997;
97 Lucht et al., 2000], and physical models [Pinty and Verstraete, 1991]. In particular, kernel-driven
98 semi-empirical models have been used frequently to generate global BRDF and albedo products.
99 Several studies have identified the so-called Ross-Thick-Li-Sparse-Reciprocal (hereinafter
100 “RTLSR”) kernel combination as the BRDF model best suited for the operational MODIS
101 BRDF/Albedo algorithm [Wanner et al., 1997; Lucht et al., 2000; Schaaf et al., 2002]. Using about
102 22,000 sets of the measured BRDFs derived from carefully selected cloud-free measurements with
103 large directional coverage from the spaceborne POLDER instrument [Bicheron and Leroy, 2000],
104 Maignan et al. [2004] evaluated the efficacy of several analytical models to reproduce these
105 observed BRDF signatures. They found that a simple kernel-driven model with only three free
106 parameters can provide an accurate representation of the BRDF. One of the best such models is
107 the three-parameter linear Ross–Li model. However, this model fails to capture the sharp
108 reflectance increase centered around the hotspot backscatter direction. From an analysis of
109 POLDER data, a correction to this model to capture the hotspot effect was proposed by [Bréon et
110 al., 2002]. By means of an explicit representation of the hotspot effect for a few degrees around
111 the backscattering direction, Maignan et al. [2004] found that the hot-spot modified RTLSR linear
112 BRDF model with three free parameters produced the best agreement with measurement. This
113 BRDF model from [Maignan et al., 2004] was referred to as the “Ross–Li–Maignan” model in
114 [Vermont et al., 2009].

115 With three linear parameters characterizing the Ross–Li model, it is a straightforward process to
116 invert the model by minimizing the Root Mean Square (hereafter RMS) difference between the
117 measurements and the modeled directional reflectances. This BRDF inversion technique has been
118 used to derive the MODIS BRDF/Albedo product [Schaaf et al., 2002]. An improvement was made
119 by Vermont et al. (2009) to correct the time series of surface reflectance derived from MODIS.
120 Using POLDER data, Bacour and Bréon [2005] retrieved the three parameters, using the modified
121 Ross–Li model, and further analyzed the variability of these parameters with vegetation cover
122 types. A common approach to derive the surface reflectance directional signatures from satellite
123 observations is to first remove the atmospheric absorption and scattering effects. This process,
124 which converts the top of the atmosphere (TOA) signal to a surface reflectance, is often called
125 “atmospheric correction”. The surface is generally taken to be Lambertian in such atmospheric
126 correction algorithms; however, it was found that without considering the BRDF effects,
127 atmosphere correction errors can reach up to 10% at certain geometries and under turbid conditions
128 [Vermote et al., 1995]. Since the mid-1980s, atmospheric correction algorithms have evolved from
129 the earlier “empirical line” and “flat-field” methods to more modern approaches based on rigorous
130 radiative transfer modeling [Gao et al., 2009]. Clearly, the accurate simulation of atmospheric and
131 surface radiative transfer is a critical element in the derivation of surface BRDF from satellite
132 measurements.

133 Several key numerical radiative transfer models (RTMs) were developed in the 1980s, and the
134 most popular RTMs in use today are usually based on discrete ordinate methods or the doubling-
135 adding technique. Following detailed mathematical studies made by Hovenier and others



136 [Hovenier and van der Mee, 1983; de Rooij and van der Stap, 1984], a general doubling-adding
137 model was developed for atmospheric radiative transfer modeling, e.g. [de Haan et al., 1987;
138 Stammes et al., 1989]. DISORT is a discrete ordinate model developed by Stammes and co-
139 workers and released for public use in 1988 [Stammes et al., 1988; Stammes et al., 2000]; a vector
140 discrete ordinate model (VDISORT) was developed later on in the 1990s [Schulz et al., 1999]. In
141 the 1980s, Siewert and colleagues made a number of detailed mathematical examinations of the
142 vector RT equations. The development of the scattering matrix in terms of generalized spherical
143 functions was reformulated in a convenient analytic manner [Siewert, 1981; Siewert, 1982;
144 Vestrucci and Siewert, 1984], and a new and elegant solution from a discrete ordinate viewpoint
145 was developed for the scalar [Siewert, 2000a] and vector [Siewert, 2000b] single-layer slab
146 models. LIDORT [Spurr et al., 2001; Spurr, 2002] and VLIDORT [Spurr, 2006] are multiple-
147 scattering multi-layer discrete ordinate scattering codes with simultaneous linearization facilities
148 for the generation of the radiation field and analytically-derived Jacobians (weighting functions or
149 partial derivatives of the radiation field with respect to any atmospheric or surface parameter).
150 SCIATRAN is a comprehensive software package for the modeling of radiative transfer processes
151 in the terrestrial atmosphere and ocean from the ultraviolet to the thermal infrared, including
152 multiple scattering processes, polarization, thermal emission and ocean–atmosphere coupling; the
153 software package contains several radiative transfer solvers including discrete-ordinate techniques
154 [Rozanov et al., 2014]. The Second Simulation of the Satellite Signal in the Solar Spectrum (6S)
155 [Vermote et al., 1997] RTM is widely used in the atmospheric correction community; 6S is based
156 on the successive orders of scattering approach (SOS) [Lenoble et al., 2007]. In this study, we will
157 use the VLIDORT RTM, which has a fully-developed supplemental code package for the
158 generation of surface BRDFs. This supplement includes a variety of BRDF kernel models (semi-
159 empirical BRDF functions developed for particular types of surfaces) that can be combined
160 linearly to that provide total BRDFs required as input for the full VLIDORT RTM calculations.
161 These kernels include the Ross–Li model both with and without the hotspot correction.

162 In the first part of this study (Section 2) we discuss the Ross-Li kernel hotspot correction in detail,
163 and present an alternative model of the hotspot correction; this new formulation is designed to
164 improve the hotspot convergence with respect to the number of cosine-azimuth Fourier terms
165 needed to represent the BRDF and also to the number of azimuth quadrature angles needed for the
166 numerical derivation of these Fourier terms. In Section 3, we investigate accuracies for
167 reconstructed BRDFs in the hotspot region, comparing our new model with older hot-spot
168 corrections. Then, using VLIDORT and the new hotspot correction model, we examine the impact
169 of atmospheric scattering on the simulated TOA-hotspot signature. Summary and conclusions are
170 given in Section 4.

171



172 2. Hotspot BRDF Models

173 2.1. RossThick-LiSparse-Reciprocal (RTLSR) BRDF model

174 Land surfaces possess complicated structural elements, making the reflective properties of such surfaces
 175 very hard to model. The geometric structure of a given land surface greatly influences its reflectance, thanks
 176 to shadowing and multiple scattering effects [Roujean et al., 1992]; this angle-dependent scattering
 177 component is called “geometric scattering”. Another structure-related scattering effect is called
 178 “volumetric scattering”, which usually consists of multiple reflections from different components within a
 179 volume and produces a minimum reflectance near nadir viewing. Scattering by trees, branches, soil layers,
 180 and snow layers are typical manifestations of volumetric scattering. These two scattering processes are
 181 usually used to characterize the surface BRDF. For example, the operational Moderate Resolution
 182 Imaging Spectroradiometer (MODIS) BRDF/Albedo product is derived based on semi-empirical
 183 kernel-driven linear BRDF models that composes of three components: an isotropic scattering
 184 term, a geometric scattering kernel, and a volumetric scattering kernel. The RossThick-LiSparse-
 185 Reciprocal (RTLSR) kernel combination has been identified as the best model suited for the
 186 operational MODIS BRDF/Albedo retrieval ([Schaaf et al., 2002] and references therein), in which
 187 the land surface reflectance function $B(\theta_i, \theta_r, \Delta\varphi)$ is represented as:

$$188 \quad B(\theta_i, \theta_r, \Delta\varphi) = P_1 K_{Lamb} + P_2 K_{geo}(\theta_i, \theta_r, \Delta\varphi, P_4, P_5) + P_3 K_{vol}(\theta_i, \theta_r, \Delta\varphi). \quad (1)$$

189 Here, θ_i and θ_r are the incident (solar) and reflected (viewing) zenith angles, and φ_i and φ_r the
 190 corresponding azimuth angles, with $\Delta\varphi = \varphi_r - \varphi_i$ the relative azimuth angle. P_1 is the Lambertian
 191 kernel amplitude with $K_{Lamb} \equiv 1$, while P_2 and P_3 are the weights of the Li-Sparse-Reciprocal
 192 geometric scattering kernel K_{geo} and the Ross-Thick volume scattering kernel K_{vol} respectively.
 193 Parameters P_4 and P_5 characterize K_{geo} and are discussed below. This 3-kernel semi-empirical
 194 model has shown surprising ability to reproduce with high accuracy the measured directional
 195 signatures of the main land surfaces; the RTLSR model is significantly better than other analytical
 196 models or combinations thereof [Maignan et al., 2004]

197 The Li-Sparse-Reciprocal geometric scattering kernel was derived from surface scattering and the
 198 theory of geometric shadow casting by [Li and Strahler, 1992], and is given by

$$199 \quad K_{geo}(\theta_i, \theta_r, \Delta\varphi, P_4, P_5) = \frac{1 + \sec\theta'_r \sec\theta'_i + \tan\theta'_r \tan\theta'_i \cos\Delta\varphi}{2} +$$

$$200 \quad \left(\frac{t - \sin t \cos t}{\pi} - 1 \right) (\sec\theta'_r + \sec\theta'_i). \quad (2)$$

$$201 \quad \cos^2 t = \left(\frac{P_4}{\sec\theta'_r + \sec\theta'_i} \right)^2 [G(\theta'_r, \theta'_i, \Delta\varphi)^2 + (\tan\theta'_r \tan\theta'_i \sin\Delta\varphi)^2]; \quad (3)$$

$$202 \quad G(\theta'_r, \theta'_i, \Delta\varphi) = \sqrt{\tan^2\theta'_r + \tan^2\theta'_i - 2\tan\theta'_r \tan\theta'_i \cos\Delta\varphi}; \quad (4)$$

$$203 \quad \tan\theta'_r = P_5 \tan\theta_r; \quad \tan\theta'_i = P_5 \tan\theta_i. \quad (5)$$

204 We note also the following expression for the scattering angle ζ :

$$205 \quad \cos\zeta = \cos\theta_r \cos\theta_i + \sin\theta_r \sin\theta_i \cos\Delta\varphi \quad (6)$$

206 Assuming a dense leaf canopy, and tree crowns that are spheroids with vertical length $2b$,
 207 horizontal width $2r$, and centroid distance h above the ground, then $P_4 = h/b$ and $P_5 = b/r$ are



208 two parameters representing the crown relative height. P_4 and P_5 can be obtained empirically,
209 and they are usually assumed to take values 2 and 1 respectively.

210 The Ross-Thick volume scattering kernel K_{vol} was derived from volume scattering radiative
211 transfer models by [Ross, 1981], and it is often referred to as “Ross thick” [Wanner et al., 1995]:

$$212 \quad K_{vol}(\theta_i, \theta_r, \Delta\varphi) = \frac{\left(\frac{\pi}{2} - \zeta\right) \cos\zeta + \sin\zeta}{\cos\theta_r' + \cos\theta_i'} - \frac{\pi}{4}. \quad (7)$$

213 Since we are using the RTLSR linear model to reproduce natural target BRDFs, it follows that the
214 three parameters will contain most of the reflectance directional information for view angles of
215 less than 60° . Theoretically, parameter P_1 and P_2 in Eq. (1) can be derived, but due to the extensive
216 variability of surface cover and biome types, there remains the practical question as to the
217 determination of the free parameters [Vermont et al., 2009], and for the MODIS BRDF/Albedo
218 product, P_1 , P_2 and P_3 are derived from MODIS measurements in a few channels. A hyperspectral
219 bidirectional reflectance (HSBR) model for land surface was developed by [Yang et al., 2020].
220 The HSBR model includes a diverse land surface BRDF database with about 40,000 spectra, stored
221 in terms of the three Ross-Li parameters. The HSBR model has been validated using the USGS
222 vegetation database and the AVIRIS reflectance product, and can be used to generate hyperspectral
223 reflectance spectra at different sensor and solar observation geometries.

224 *2.2. Hot-Spot models, including an improved formulation*

225 Based on an analysis of POLDER measurements, Bréon et al.[2002] found that the hotspot
226 directional signature is proportional to $(1 + \zeta/\zeta_0)^{-1}$, where ζ_0 is the hotspot halfwidth that can
227 be related to the ratio of scattering element size and canopy vertical density. This hotspot modeling
228 has been validated against measurements acquired with the spaceborne POLDER instrument with
229 a very high directional resolution, i.e. on the order of 0.3° [Bréon et al., 2002]. Maignan et al.[
230 2004] brought this hotspot correction into the Ross-Li model, and re-wrote the Ross thick kernel
231 with hotspot correction as:

$$232 \quad K_{vol} = \frac{4}{3\pi} \frac{\left(\frac{\pi}{2} - \zeta\right) \cos\zeta + \sin\zeta}{\cos\theta_r' + \cos\theta_i'} \left(1 + \frac{1}{1 + \zeta/\zeta_0}\right) - \frac{1}{3}. \quad (8)$$

233 We note here that there is a difference of a factor of $\frac{4}{3\pi}$ between Eqs. (7) and (8). Bréon et al. [2002]
234 indicated that ζ_0 is generally in a small range between 0.8° to 2° , while some dispersion occurs in
235 the range 1° – 4° for scenarios classified as forest and desert types in the International Geosphere-
236 Biosphere Program (IGBP) system. For the sake of simplicity, and to avoid the addition of a free
237 parameter in the BRDF modeling, Maignan et al.[2004] suggested setting a constant value of $\zeta_0 =$
238 1.5° . The version of the RTLSR model which accounts for the hotspot signature using Eq. (8) will
239 be denoted as RossThickHT-M in this paper. Using multidirectional PARASOL (Polarization &
240 Anisotropy of Reflectances for Atmospheric Sciences coupled with Observations from a
241 Lidar) data at coarse resolution (6 km) over a large set of representative targets, Maignan et
242 al.[2004] showed that the simple three-parameter model permits accurate representation of the
243 BRDFs.

244 Another hotspot correction was developed by Chen and Cihlar[1997] as a negative exponential
245 function, and Jiao et al. [2013] brought this latter correction to the Ross-Li model, as follows:



$$246 \quad K_{vol} = \frac{4}{3\pi} \frac{(\frac{\pi}{2}-z) \cos \zeta + \sin \zeta}{\cos \theta'_r + \cos \theta'_i} (1 + C_1 e^{(-\frac{\zeta}{\pi}) C_2}) - \frac{1}{3}. \quad (9)$$

247 Here, C_1 is physically related to the difference between the spectral reflectance of foliage and the
 248 background, controlling the height of the hotspot; C_2 is related to the ratio of canopy height to the
 249 size of the predominant canopy structure, determining the width of the hotspot. We found that we
 250 can simply set C_2 to be ζ_0 . We remark that ζ_0 is given in radians in Eq. (8) and in degrees in Eq.
 251 (9). However, Bréon et al. [2002] determined that observed hotspot signatures are better fitted with
 252 a function of $(1 + \zeta/\zeta_0)^{-1}$ rather than with a negative exponential that is often used for hotspot
 253 modeling.

254 In this paper, we denote the version of the RTLSR model that accounts for the Hot-Spot process
 255 using Eq. (9) as RossThickHT-C. Some validation to the RossThickHT-C model has been made
 256 by Jiao et al. [2013]. Although one advantage of RossThickHT-C model is the ability to use
 257 parameter C_1 to adjust the amplitude of hotspot [Jiao et al., 2013], such an adjustment can be also
 258 easily made by adding one parameter in the correction term in Eq. (8), i.e. to change $(1 + \zeta/\zeta_0)^{-1}$
 259 to $C_1/(1 + \zeta/\zeta_0)$. With this in mind, our effort will focus on an improvement in the Ross-Thick
 260 BRDF kernel, starting with the baseline model of Maignan et al. [2004].

261 A number of kernel BRDF models have been incorporated in the LIDORT and VLIDORT RTMs,
 262 including the RTLSR model and the RossThickHT-M model. In VLIDORT (and this applies
 263 equally to other polarized radiative transfer models). it is necessary to develop solutions for the
 264 radiation fields in terms of Fourier cosine and sine azimuth series; the same considerations apply
 265 to the BRDFs. For scalar kernel models without polarization, only the Fourier cosine series is
 266 needed. The Fourier components of the total BRDF are calculated through:

$$267 \quad B^m(\mu, \mu') = \frac{1}{2\pi} \int_0^{2\pi} B(\mu, \mu', \varphi) \cos m\varphi d\varphi. \quad (10)$$

268 Integration over the azimuth angle is done by double numerical quadrature over the ranges $[0, \pi]$
 269 and $[-\pi, 0]$. The number of BRDF azimuth quadrature abscissa (N_{BRDF}) should be set to at least
 270 100 in order to obtain a numerical accuracy of 10^{-4} for most kernels considered in the VLIDORT
 271 BRDF supplement [Spurr, 2004]. However, at and near the hotspot region, many more quadrature
 272 points and Fourier terms ($N_{FOURIER}$) will be needed, as we will demonstrate below. Indeed, Lorente
 273 et al. (2018) found that in order to reach an accuracy of 10^{-3} over the hotspot region, 720 Gaussian
 274 points were needed for the azimuth integration and 300 Fourier terms for the reconstruction of any
 275 BRDF in terms of its Fourier components; they also determined that, in the final implementation
 276 of the surface BRDF in the DAK radiative transfer model (Doubling–Adding KNMI, [Lorente et
 277 al., 2017]) designed to perform with optimal simulation time, some 100 Fourier terms and 360
 278 Gaussian points were necessary for proper hotspot characterization.

279 These values of N_{BRDF} and $N_{FOURIER}$ are still unacceptably high, and in order to use VLIDORT to
 280 simulate the hotspot signature with a modest number of discrete ordinates, we have made an
 281 empirical modification to the hotspot correction in the RossThickHT-M model by using the
 282 function $\sin^x(\zeta) * \frac{1}{\sin^x(\zeta_0)}$ to replace ζ/ζ_0 , where $x = 2 + \sin(\theta'_r)$. Thus:

$$283 \quad K_{vol} = \frac{4}{3\pi} \frac{(\frac{\pi}{2}-\zeta) \cos \zeta + \sin \zeta}{\cos \theta'_r + \cos \theta'_i} (1 + \frac{1}{1 + \sin^x(\zeta) * \frac{1}{\sin^x(\zeta_0)}}) - \frac{1}{3}. \quad (11)$$



284 We use the nomenclature RossThickHT-X to indicate the model with the hotspot correction given
285 in Eq. (11).

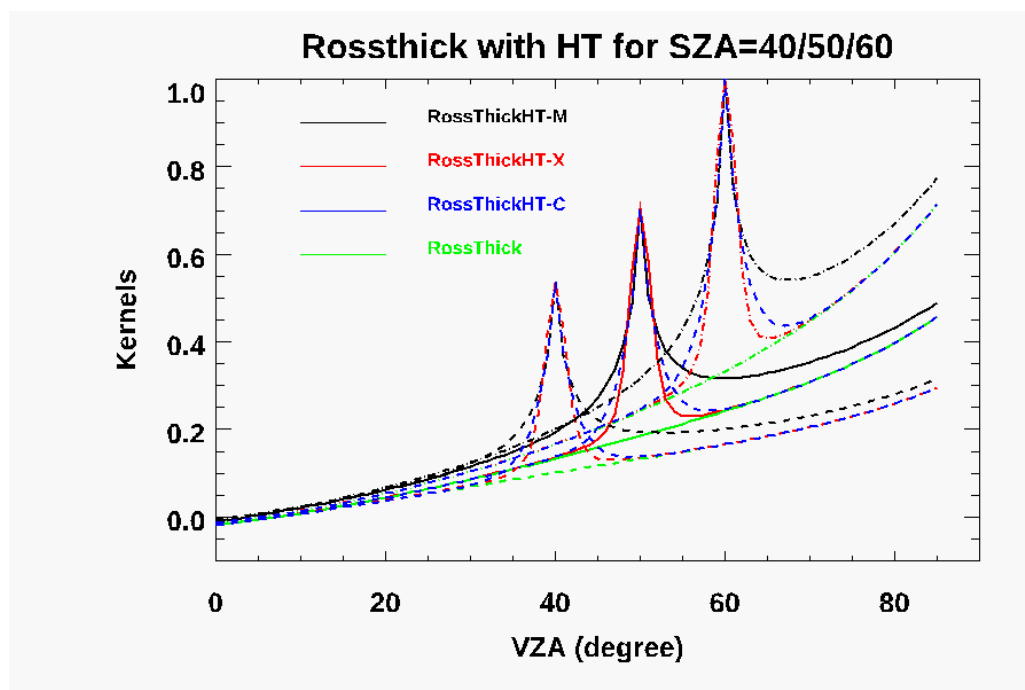
286 In the next section, we first examine the above sets of hotspot signatures, with particular emphasis
287 on the accuracy of reconstructed BRDFs in terms of the two numerical indices N_{BRDF} and N_{FOURIER} .
288 We then determine the impact of a scattering atmosphere, using these hotspot BRDF quantities as
289 inputs to VLIDORT calculations based on standard-atmosphere pressure/temperature profiles with
290 Rayleigh scattering and aerosols in the form of an optically-constant layer from the surface to 6.5
291 km having total optical depth of 0.2; aerosol optical properties are taken from a “continental
292 pollution” aerosol type [Hess et al., 1998], with lognormal poly-disperse size distribution.



293 3. Results and Discussion

294 3.1 Hotspot Comparisons and BRDF reconstruction accuracy

295 Figure 1 shows a comparison of the volume-scattering kernel for the three hotspot models,
296 RossThickHT-X, RossThickHT-C and RossThickHT-M, with actual hotspots at three different
297 solar zenith angles in the principal-plane backscatter direction. For reference, the original
298 RossThick kernel is also plotted. Hotspot peaks from the three models are the same, and the hotspot
299 peak is higher and narrower at larger zenith angles. Major differences between the three models
300 are outside the hotspot region. As indicated by [Jiao et al., 2013], one asset of RossThickHT-C is
301 that it better matches the RossThick model in regions beyond the hotspot, while on the other hand,
302 there remain some differences between the RossThickHT-M and RossThick model away from the
303 hotspot. Our new model RossThickHT-X has the same advantage as RossThickHT-C, in that
304 agreement with the standard RossThick model beyond the hotspot region is accurate.



305
306

307 **Figure 1.** Four Ross-Thick volume scattering kernels for a range of reflection zenith angles,
308 and for three solar incident angles as indicated; reflectance is in the principal plane.

309 The major advantage of our new hotspot correction model is the rapid convergence for
310 reconstruction. Table 1 lists values of N_{BRDF} (number of azimuth quadrature abscissae) and
311 $N_{FOURIER}$ (number of Fourier Terms) that are needed to reconstruct the BRDF to different accuracy
312 levels; the accuracy is computed as the relative difference of the reconstructed BRDF to its exact
313 value at the hotspot. Compared to numbers required for the RossThickHT-M, values of N_{BRDF} and
314 $N_{FOURIER}$ for the RossThickHT-X case are 10 to 60 times smaller (Table 1). These results show
315 that RossThickHT-X converges much faster than RossThickHT-M. We see also that convergence



316 of RossThickHT-C is somewhat faster than that for RossThickHT-M but still much slower than
 317 that for RossThickHT-X.

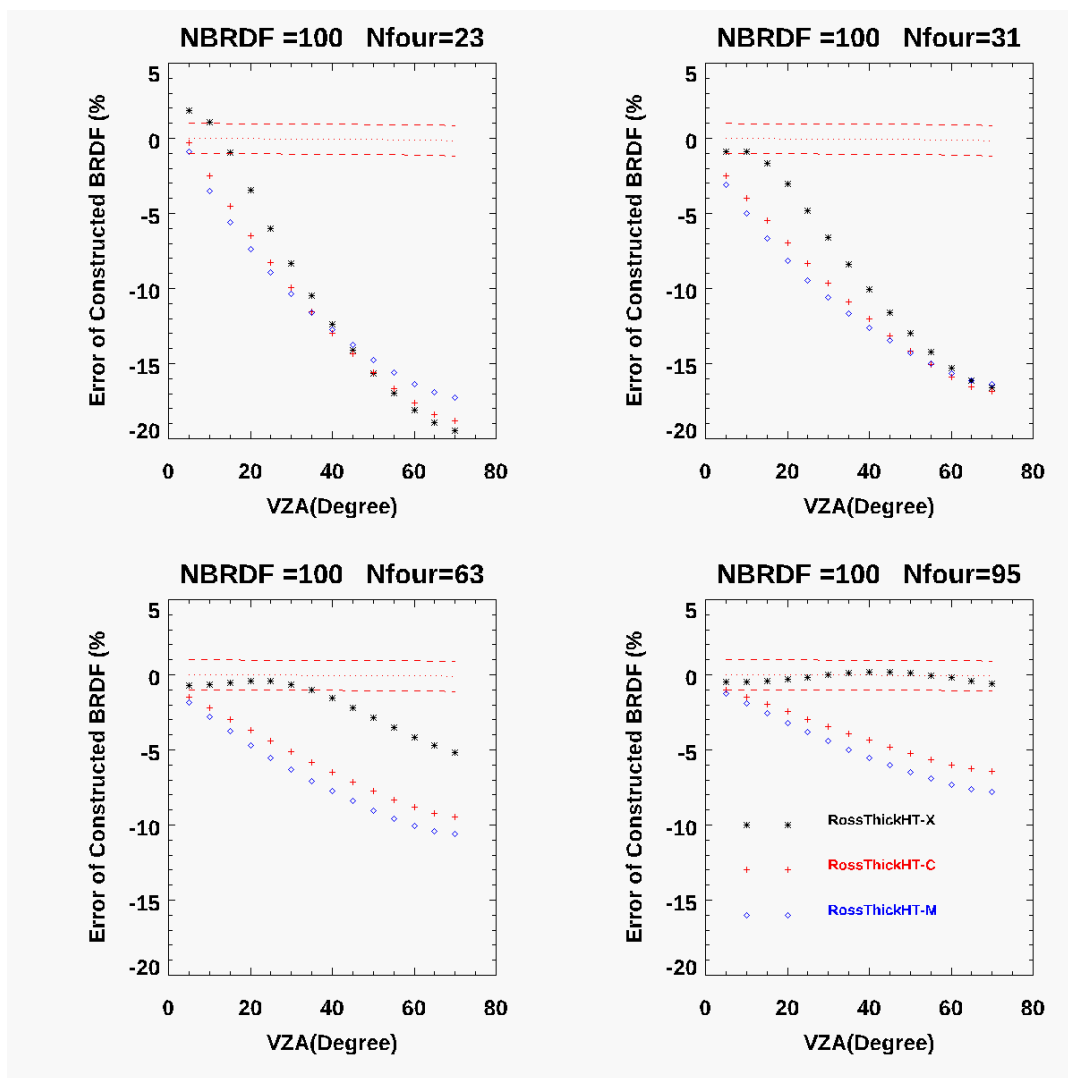
318 **Table 1.** Values of N_{BRDF} and $N_{FOURIER}$ needed to reconstruct a hotspot with $\zeta_0 = 1.5^\circ$.

		RossThickHT-M		RossThickHT-X		RossThickHT-C	
#	Accuracy (%)	NBRDF	N_FOURIER	NBRDF	N_FOURIER	NBRDF	N_FOURIER
1	1	2810	1402	278	139	1578	789
2	0.5	5620	2807	324	162	3158	1579
3	0.4	7020	3509	338	169	3948	1974
4	0.3	9360	4679	356	178	5264	2632
4	0.2	14040	7019	382	191	7896	3948
5	0.1	28080	14039	428	214	15794	7897

319 While both numbers are necessary for the reconstructed BRDF accuracy, the main impact comes
 320 from the number of Fourier terms $N_{FOURIER}$ used, when the value of N_{BRDF} is twice (or more) that
 321 of $N_{FOURIER}$. In Figure 2, using a fixed value $N_{BRDF} = 100$ for the RossThickHT-M, RossThickHT-
 322 C and RossThickHT-X models, we show the dependence of the relative error of the reconstructed
 323 BRDF on the solar zenith angle for four different values of $N_{FOURIER}$. Choices of $N_{FOURIER}$ (23, 31,
 324 63 and 95) correspond to values 12, 16, 32 and 48 for the number $N_{STREAMS}$ (number of half-space
 325 polar discrete ordinates) used in VLIDORT ($N_{FOURIER} = 2N_{STREAMS} - 1$). In this example, also used
 326 by [Lorente et al., 2018] (their Figure 6), the BRDF represents a vegetated surface over Amazonia
 327 at wavelength 758 nm with free parameters $[P_1, P_2, P_3] = [0.36, 0.24, 0.03]$ taken from MODIS
 328 band 2 (841–876 nm) to account for the increase in surface reflectivity near 700 nm.

329 Overall, the error decreases with increasing values of $N_{FOURIER}$. The error also increases with those
 330 viewing angles at which the hotspot occurs, since the hotspot peaks are higher and narrower for
 331 larger viewing angles. Errors for all three models are large when $N_{FOURIER}$ is as small as 23. The
 332 advantage of RossThickHT-X starts to show when $N_{FOURIER}$ increases to 31, but this is not
 333 significant when the hotspot viewing angle is larger than 45° . When $N_{FOURIER}$ is set to 95, the
 334 performance of RossThickHT-X is much better than that for the other two models; the error is less
 335 than 1% even for large viewing hotspot angles, whereas the corresponding errors using
 336 RossThickHT-M or RossThickHT-C are still at the 5-8% level for hotspots at viewing angles
 337 larger than 30° . Overall, the error with RossThickHT-C is slightly smaller than that for
 338 RossThickHT-M.

339



340

341

342

343

344

Figure 2. Accuracy of Fourier-reconstructed BRDFs relative to their exact values, for the three Ross-Li models. $N_{BRDF} = 100$, with $N_{FOURIER}$ set to four different values as indicated. Surface BRDF parameters represent a vegetated surface over Amazonia at 758 nm, with $[P_1, P_2, P_3] = [0.36, 0.24, 0.03]$.

345

346

347

348

349

350

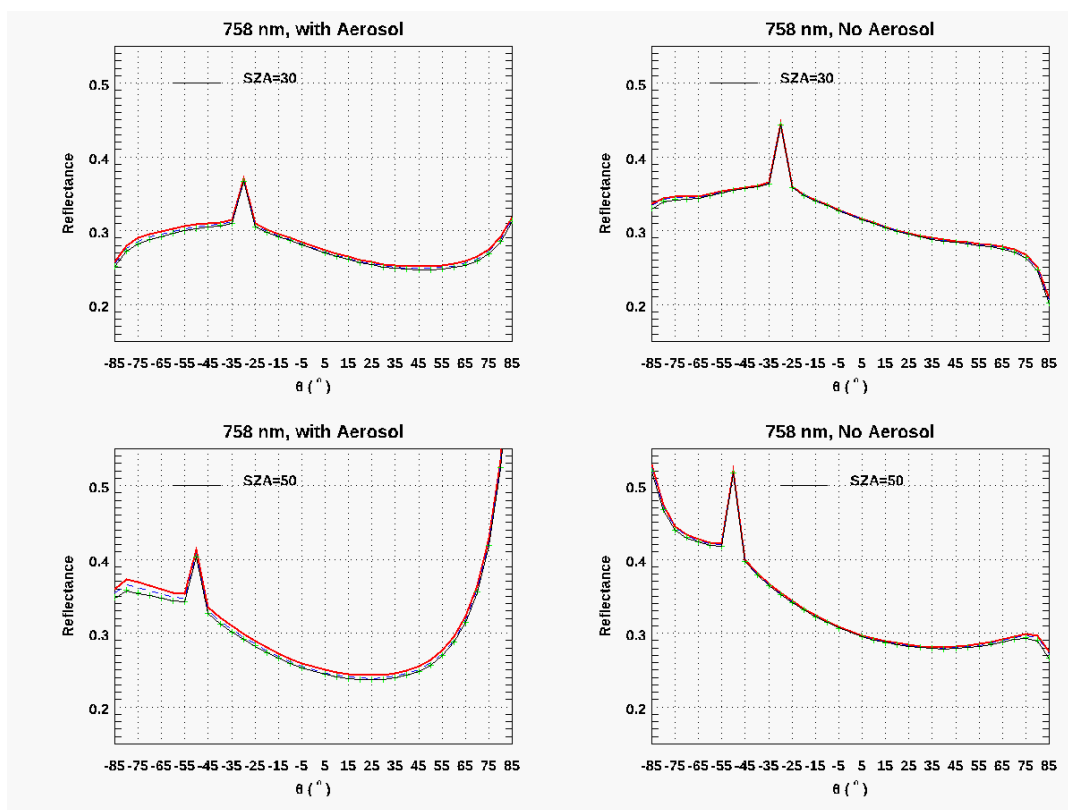
351

352

Next we examine simulated TOA reflectances at 758 nm with the three hotspot models providing inputs to the main VLIDORT RT calculations. We again set $N_{BRDF} = 100$ and $N_{STREAMS} = 12, 16, 32$ and 48. Results are shown in Figure 3 for two solar zenith angles. The hotspot signature is evident at 30° (upper panels) and 50° (lower panels), and the peak signature with aerosols present is higher than that without aerosol. The widths of the hotspots in Figure 3 are very similar, confirming the argument of [Powers and Gerstl, 1988] that the hotspot width is expected to be relatively invariant to atmospheric perturbations. Lines of different colors correspond to simulations using different values of $N_{STREAMS}$; in general, differences between these lines are pretty small, especially in the

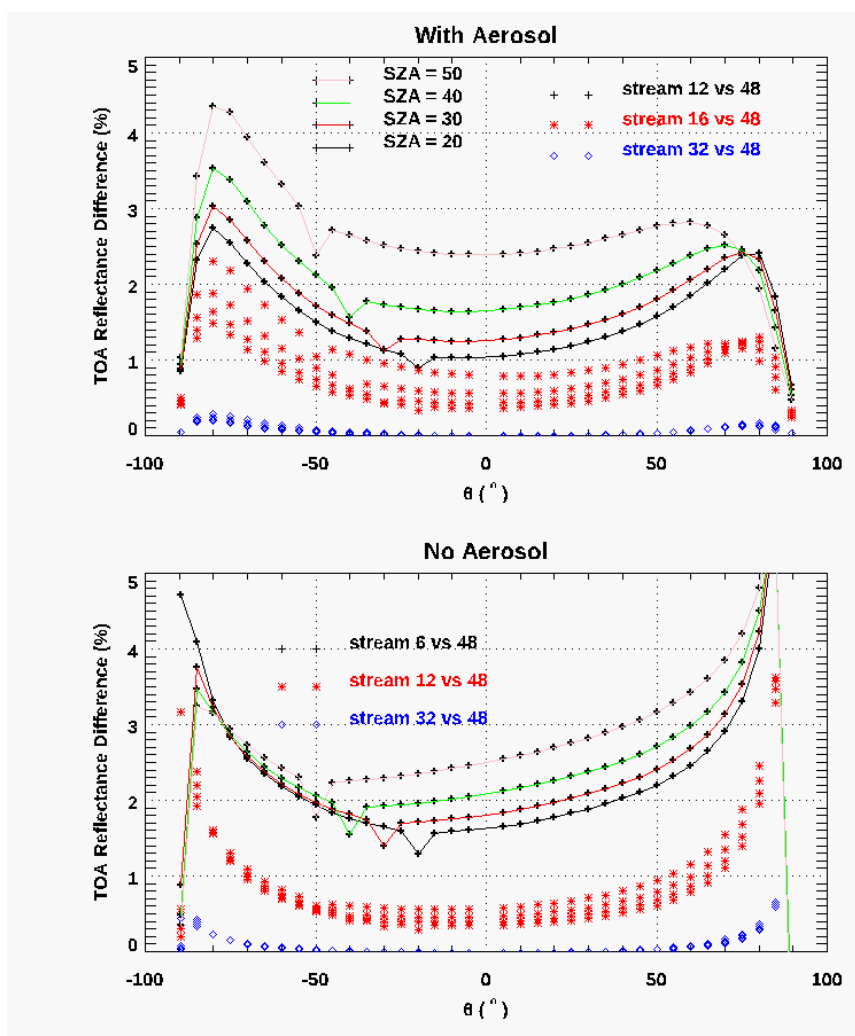


353 atmosphere without aerosol and when the viewing angle is less than 60° . To better illustrate
354 patterns in TOA reflectance values using different values N_{STREAMS} , we used the simulated
355 reflectances obtained with $N_{\text{STREAMS}} = 48$ as the reference, and the results of this comparison are
356 shown in Figure 4.



357

358 **Figure 3.** TOA reflectance as a function of viewing zenith angle, simulated by VLIDORT at 758
359 nm with a Ross-Li surface BRDF model with hotspot correction RossThickHT-X. Geometries
360 are in the principal plane for two solar zenith angles as indicated, and results were obtained with
361 and without aerosol. Surface BRDF parameters represent a vegetated surface over Amazonia at
362 758 nm with $(P_1, P_2, P_3) = (0.36, 0.24, 0.03)$. The red solid line represents the simulation N_{STREAMS}
363 $= 12$, blue dashed line is for $N_{\text{STREAMS}} = 16$, with the remaining lines for $N_{\text{STREAMS}} = 32$ (green)
364 and $N_{\text{STREAMS}} = 48$ (dark); the latter two lines are almost aligned.



365

366

367

368

Figure 4. Same set-ups as Figure 3, but now plotting the TOA reflectance differences with four solar zenith angles as indicated.

369

370

371

372

373

374

375

376

From Figure 4 it is evident that relative differences in TOA reflectances for an atmosphere with aerosols are larger than those for the atmosphere without aerosols. As the typical viewing angle range for BRDF kernels is mostly within 60° , we will focus on these differences for viewing angles $< 60^\circ$. In the upper panel we see that TOA differences (comparing $N_{\text{STREAMS}} = 12$ with $N_{\text{STREAMS}} = 48$) increase with solar zenith angle; the difference at $\text{SZA} = 50^\circ$ is almost double than that at $\text{SZA} = 20^\circ$. The relative difference in percentage at the hotspot region is smaller than beyond hotspot, which is easy to understand as the absolute value of the TOA reflectance at the hotspot is larger. In both cases with and without aerosol, TOA reflectance differences (comparing N_{STREAMS}



377 = 32 with $N_{\text{STREAMS}} = 48$) are very small; VLIDORT simulations with $N_{\text{STREAMS}} = 32$ are accurate
378 enough in this case.

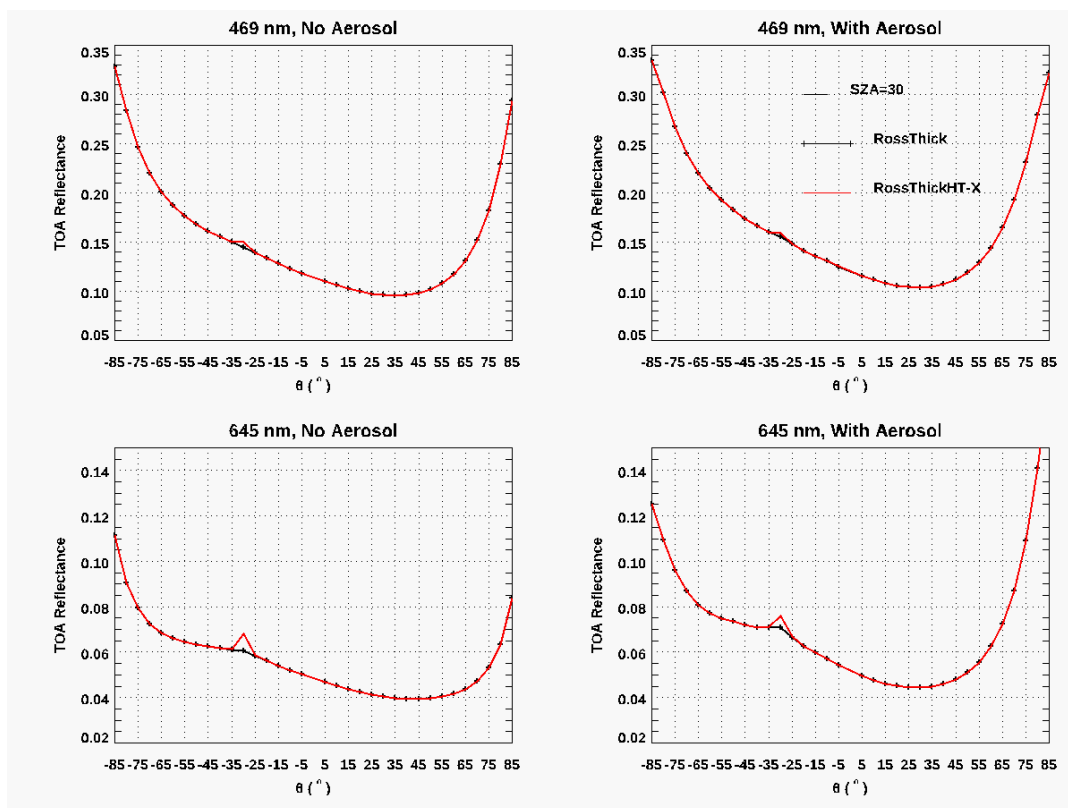
379 For the atmosphere with aerosol, the bias in simulated TOA reflectances using $N_{\text{STREAMS}} = 16$
380 (relative to $N_{\text{STREAMS}} = 48$) is 0.5-1.0%. In the clear atmosphere without aerosol, the bias of using
381 $N_{\text{STREAMS}} = 6$ can be in the region 2-3%, but the bias with $N_{\text{STREAMS}} = 12$ is around 0.5%,
382 suggesting that the setting for N_{STREAMS} should be 12 or higher in a Rayleigh atmosphere overlying
383 a hotspot surface.

384 As noted already, $N_{\text{FOURIER}} = 2N_{\text{STREAMS}} - 1$. Compared to the value of N_{FOURIER} needed for
385 reconstruction of surface BRDFs near the hotspot (Table 1), that is, $N_{\text{FOURIER}} = 139-162$ for an
386 accuracy of 0.5-1.0%, the values of $N_{\text{FOURIER}} = 23$ (for the Rayleigh scenario) and $N_{\text{FOURIER}} = 63$
387 (for the atmosphere with aerosol) needed for full VLIDORT RT simulations are much smaller.
388 The reason for this reduction lies with the separation in VLIDORT between the first order (FO:
389 single scattering and direct reflectance) calculations and the multiple-scatter (MS) calculations in
390 VLIDORT. The first-order calculation in VLIDORT is always done with full accuracy with solar
391 beam and line-of-sight attenuations treated for a curved atmosphere, and with an exact value for
392 the surface BRDF used to calculate the “direct-bounce” reflectance (which is very often the
393 dominant contribution from the surface). No Fourier reconstruction is necessary for this
394 contribution. For the MS contribution, multiple scatter is treated using Fourier cosine/sine azimuth
395 expansions and associated Fourier terms for both the truncated phase matrix for scattering and the
396 diffuse-field BRDF contributions. The important point to note here is the use of the exact BRDF
397 for the direct-bounce contribution in VLIDORT; RT models without this FO/MS separation will
398 be constrained by the need to use a Fourier-expanded reconstruction for the direct-bounce BRDF
399 contribution.

400 The results shown in Figures 3-4 are confined to a single standard atmosphere and aerosol model.
401 In the next section below, we use VLIDORT simulations to investigate the impact of scattering on
402 hotspot signatures. For this study, we choose $N_{\text{BRDF}} = 200$ and $N_{\text{STREAMS}} = 32$; this should be
403 conservative enough to avoid any uncertainty associated with the use of surface BRDFs and the
404 choice of stream numbers in VLIDORT.

405 *3.2. Impact of scattering on the hotspot signature at TOA*

406 Here we use the three parameters $(P_1, P_2, P_3) = (0.0399, 0.0245, 0.0072)$ for the RTLSR surface
407 BRDF model. These are the spatially averaged parameters from MODIS (BRDF/albedo product
408 MCD43A1) band 3 (459–479 nm) over Amazonia (latitude $5^\circ \text{ N} - 10^\circ \text{ S}$, longitude $60 - 70^\circ \text{ W}$)
409 for March 2008 [Lorente et al., 2018]. TOA reflectances are calculated as a function of viewing
410 zenith angle in the principal plane, with the solar zenith angle set at 30° (Figure 5). In this
411 experiment, two calculations are plotted, one using the new hotspot correction model,
412 RossThickHT-X, and the other using the RTLSR BRDF model without a hotspot correction. From
413 Figure 5 it is clear that the TOA-hotspot signature at 469 nm is very small, likely due to the
414 influence of stronger Rayleigh scattering. The addition of aerosol scattering further reduces the
415 hotspot signature at SZA 30° and it is hard to discriminate the TOA reflectance difference between
416 the runs with and without hotspot correction. This observation agrees with the results from [Bréon
417 et al., 2002], in which it was noted that no significant hotspot signature has been observed when
418 the surface reflectance is very small, as in the blue channel or over the ocean. For the longer
419 wavelength at 645 nm, the TOA-hotspot signature is obvious, and the addition of aerosol scattering
420 reduces the hotspot signature slightly compared to the situation with molecular scattering only.



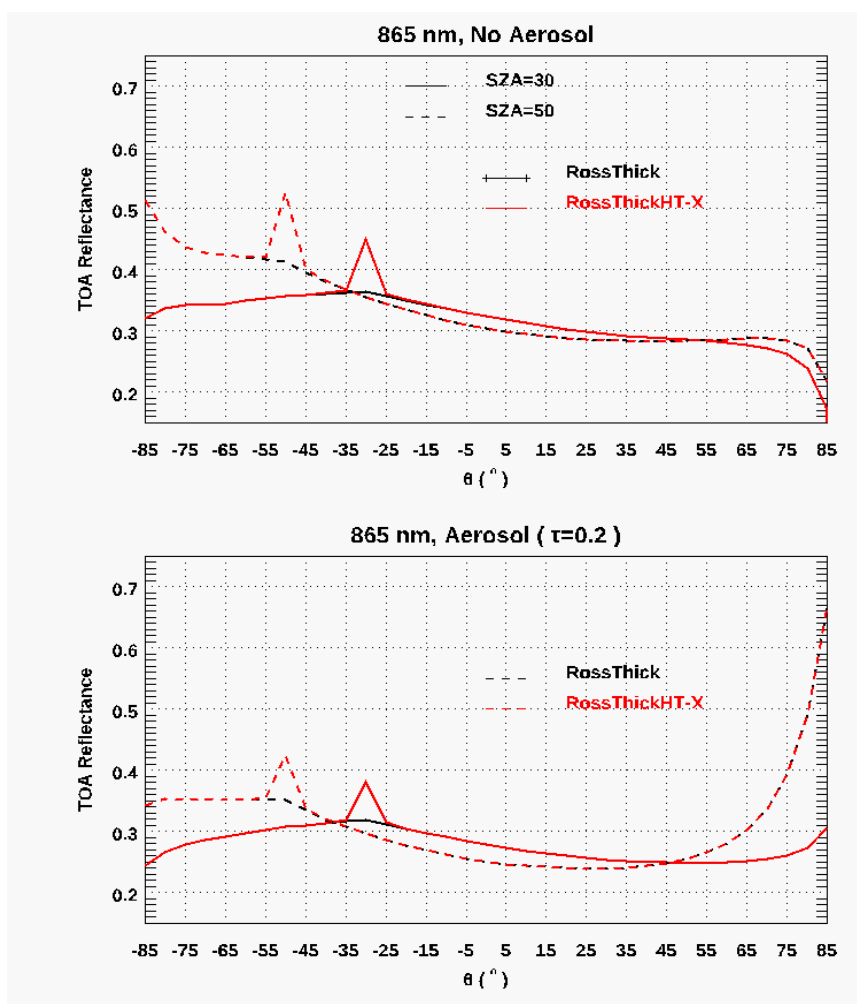
421
422

423 **Figure 5.** VLIDORT TOA reflectances as a function of viewing zenith angle with solar angle 30° in
424 the principal plane, at 469 and 645 nm using a Ross-Li surface BRDF model with hotspot correction
425 RossThickHT-X, and with and without aerosol. The aerosol model used is the same as in Figure 3,
426 with optical depth 0.2. Surface BRDF parameters represent a vegetated surface over Amazonia with
427 $(P_1, P_2, P_3) = (0.0399, 0.0245, 0.0072)$.

428 We also examine the hotspot signatures in 765 and 865 nm, two wavelengths used in POLDER
429 data analysis. The three linear weighting parameters in the BRDF model are $(P_1, P_2, P_3) = (0.36,$
430 $0.24, 0.03)$, which is the same set as that used by [Lorente et al., 2018]. As noted already, these
431 are taken from MODIS band 2 (841–876 nm) to account for the “red-edge” increase in surface
432 reflectivity near 700 nm (e.g. [Tilstra et al., 2017]). To test the representativeness of band 2 at 758
433 nm, Lorente et al.[2018] scaled the parameters from band 3 (459–479 nm) using the ratio of
434 reflectances at 772 nm and 469 nm; they found that differences with parameters taken from
435 MODIS band 2 were negligible. Since we would like to focus on the difference of the impact of
436 atmospheric scattering on the hotspot signatures at 758 and 865 nm, we have chosen to use the
437 same two sets of surface BRDF parameters. The results are plotted in Figures 6 and 7. To highlight
438 the differences caused by the $3\pi/4$ factor normalizing the volume-scattering kernels K_{vol} (see note
439 in Section 2.2), we have added in Figure 7 two simulated TOA reflectances, one based on the
440 original hotspot correction model from Maignan et al. [2004] (RossThickHT-M) and the other
441 using the BRDF noted in the paper of Lorente et al. [2018] (indicated by “RossThickHT-L”).

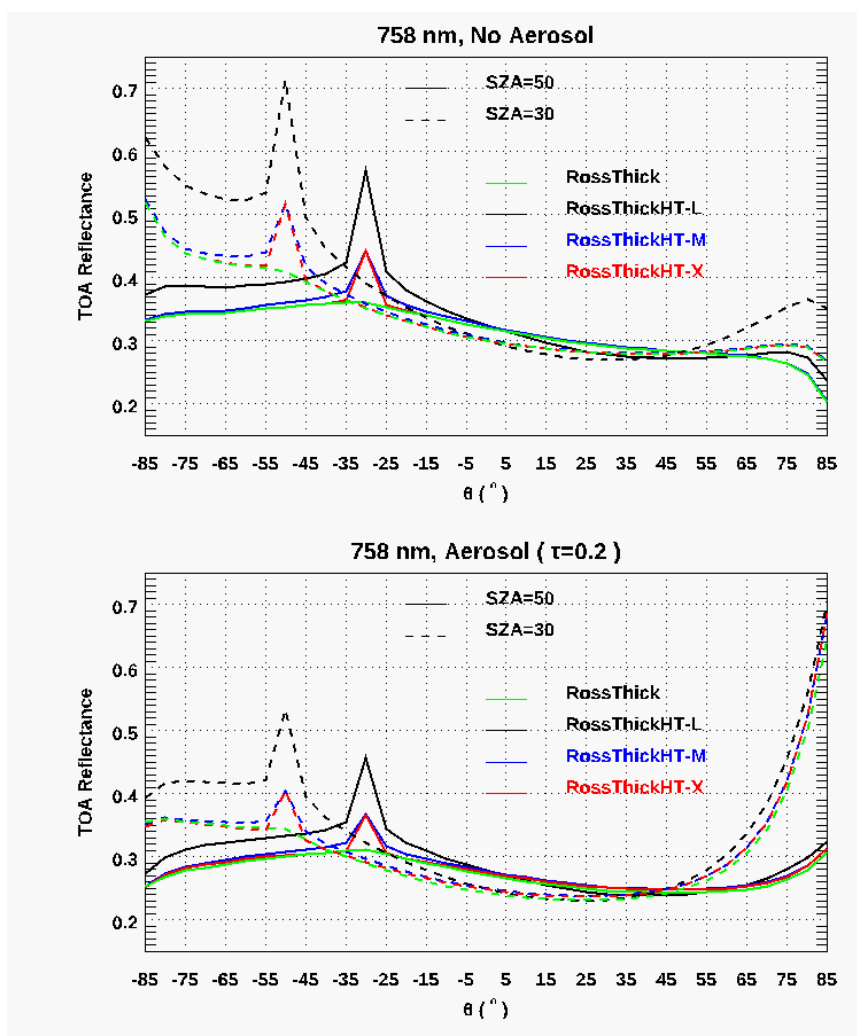


442 Compared to Figure 5, much larger TOA-hotspot signatures at both 865 and 758 nm are evident
443 in Figures 6 and 7 respectively, and they are slightly larger at $\text{SZA}=50^\circ$ than at $\text{SZA}=30^\circ$. As
444 expected, in the scattering region beyond the hotspot ($\pm 5^\circ$), the TOA reflectance using
445 RossThickHT-X agrees very well with that using the original RossThick model. However, from
446 Figure 7, we see that the simulated reflectance using RossThickHT-M is slightly larger than that
447 using RossThick model even in a region of $\pm 15^\circ$ beyond the hotspot, particularly in the large
448 viewing angles in the forward direction. In the region of $\pm 5^\circ$ to $\pm 15^\circ$ beyond the hotspot, the
449 simulated reflectance using RossThickHT-M is clearly larger than that using RossThick and
450 RossThickHT-X.
451



452
453
454
455

Figure 6. Same as Figure 5 but results are calculated at 865 nm for solar zenith angles 30° and 50° . Surface BRDF parameters represent a vegetated surface over Amazonia with $(P_1, P_2, P_3) = (0.36, 0.24, 0.03)$.



456

457 **Figure 7.** Similar to Figure 6 but results calculated at wavelength 758 nm. For comparison, we
 458 have added simulated TOA reflectances using the original hotspot correction model from
 459 [Maignan et al., 2004] (RossThickHT-M) and again using the model in [Lorente et al., 2018],
 460 which is a factor of $4\pi/3$ times larger than RossThickHT-M in the hotspot region and is denoted
 461 here as RossThickHT-L.

462 To better quantify the hotspot effect and the impact due to scattering in the atmosphere, we define
 463 the “hotspot amplitude” as the difference between the TOA reflectance at the hotspot and the
 464 corresponding TOA reflectance calculated without hotspot correction, namely:

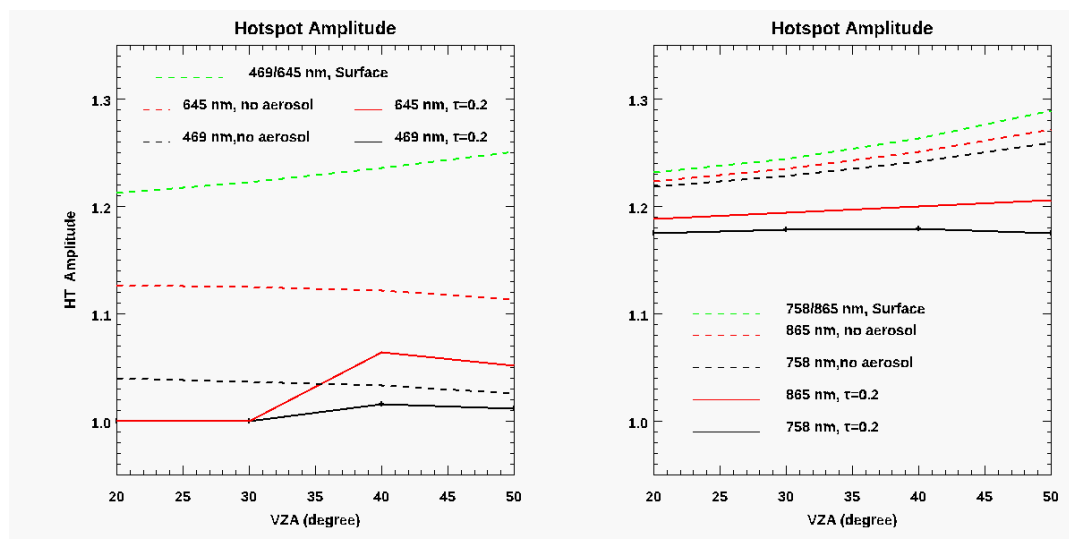
465

$$HT_{Amplitude} = \frac{R(\theta_0, \theta, \varphi = 180, \text{RossThickHT} - Li)}{R(\theta_0, \theta, \varphi = 180, \text{RossThick} - Li)}$$

466 The impacts of molecular and aerosol scattering on these amplitudes are illustrated in Figure 8 for
 467 a range of hotspot viewing angles and for four wavelengths. For comparison, the hotspot



468 amplitudes at the surface are also plotted. From Figure 8, it is evident that scattering in the
469 atmosphere smooths out the hotspot signature at TOA, and the impact of scattering is much larger
470 in the visible compare with that in the near-infrared part of the spectrum. Even in the visible, the
471 amplitude of the hotspot signature at 469 nm is much smaller than that at 645 nm. Similarly, the
472 amplitude in 758 nm is smaller than that at 865nm. These simulated results agree well with the
473 analysis of POLDER data by [Bréon et al., 2002]; at 440 nm, they found that the amplitude of the
474 hotspot signature is very small, confirming that the atmospheric contribution to the reflectance
475 increase at the backscattering direction is negligible. The much larger amplitudes observed at 758
476 nm and 865 nm also confirm the findings by [Maignan et al., 2004], who showed that near-infrared
477 measurements are preferred to those in the visible, not only because of the larger-amplitude
478 directional effects but also because of the lower atmospheric perturbation. Indeed, Maignan et
479 al.[2004] suggested that near-infrared measurement data is better suited for the evaluation of
480 different BRDF models. From Figure 8 we can also see that in the near-infrared, the amplitude of
481 the hotspot signature increases with the zenith angle (right panel); however, the angular
482 dependencies in the surface hotspot and the TOA hotspot are almost opposite in the visible,
483 especially for an atmosphere without aerosols.



484

485 **Figure 8.** Comparison of hotspot amplitudes at the TOA for an atmosphere with and without
486 aerosols in visible (469 and 645 nm, left panel) and near-infrared (658 and 865 nm, right panel).
487 Hotspot amplitudes at the surface are computed using the differences between the RossThickHT-
488 Li and RossThick-Li BRDF models.

489 In the processing of POLDER data done by [Bréon et al., 2002] and [Maignan et al., 2004], only
490 molecular scattering to first order was taken into account for the atmospheric correction. As there
491 is no correction for the effects of aerosol scattering or the coupling of surface reflectance with
492 molecular scattering, absolute values of the reflectances may not be fully representative of the
493 surface for POLDER [Bréon et al., 2002]. From our simulations shown in Figure 8, the amplitude
494 of the hotspot signature with aerosol scattering included is smaller than that without aerosol,
495 suggesting that the results from POLDER [Bréon et al., 2002] might underestimate the amplitude
496 of hotspot signature at the surface.



497 A final issue is related to a factor difference that exists between the equation of [Lorente et al.,
498 2018] (i.e. their Eq. A1) with our Eq. (8), which is the one used in [Maignan et al., 2004]. The one
499 used by [Lorente et al., 2018] is $3\pi/4$ times larger; this discrepancy results in a TOA-hotspot
500 signature more than twice as large, as shown in Figure 7. This factor difference is the main reason
501 that the TOA-hotspot signatures shown by [Lorente et al., 2018]their Figure 5) at 469 and 645 nm
502 are higher than the ones observed in this paper. In addition, as seen in [Lorente et al., 2018] (their
503 Figure 5), the lower TOA-hotspot signature generated by LIDORT (as opposed to those from the
504 other two RTMs) is likely due to the deployment of an older version of LIDORT that did not
505 include the hotspot correction. From the upper panel of Figure 7, it is evident that the hotspot peak
506 using RossThickHT-L seems too high, particularly for the hotspot occurring at 50° . From the
507 analysis of POLDER data, Bréon et al.[2002] found that the hotspot reflectance amplitude is
508 generally of the order 0.10 – 0.20 at 865 nm and 0.03 – 0.18 at 670 nm, although the full range of
509 values is wide. Therefore, we think that the use of an equation with a factor of $3\pi/4$ discrepancy is
510 likely to overestimate the hotspot effect, and we caution users to be careful to check the equations
511 for the presence of this $3\pi/4$ factor, even when using MODIS BRDF products.



512 4. Summary and Conclusions

513 In remote sensing, it is common practice to deploy a simple kernel-driven semi-empirical model
514 with three free parameters to represent land surface BRDFs (excepting snow and ice); the best
515 model is the RossThick/LiSparse combination with a correction to account for the hotspot
516 [Maignan et al., 2004]. In our study, we modified this BRDF model to improve convergence of
517 the Fourier azimuth series decomposition, and using this new hotspot correction, we further studied
518 the impact of scattering on the atmospheric hotspot signature using the VLIDORT RTM.

519 With the improved hotspot correction, we found that the numbers of Gaussian points (N_{BRDF}) and
520 Fourier Terms (N_{FOURIER}) are more than 10 times smaller than those needed with the original
521 hotspot model from Maignan et al. [2004]; this makes our BRDF model much more practical for
522 use with VLIDORT to simulate the hotspot signature at the TOA. We also showed the new hotspot
523 model agrees very well with the original RossThick model away the hotspot region, thus allowing
524 the use of this single model in the condition with and without hotspot.

525 We carried out a number of investigations on the impact of molecular and aerosol scattering on
526 the hotspot signature at the TOA. TOA reflectances were calculated for different solar and viewing
527 angles and at four wavelengths; the main findings from our study are:

- 528 1. In agreement with previous analysis using POLDER measurement data, hotspot signatures
529 in the near-infrared are larger than those in the visible.
- 530 2. Also in agreement with the POLDER study, the hotspot amplitudes at TOA and the surface
531 both increase with solar zenith angle in the near-infrared; however, at 469 and 645 nm, this
532 increase with solar zenith angle is not obvious at TOA.
- 533 3. Scattering by molecules and aerosols in the atmosphere tends to smooth out the hotspot
534 signature at TOA, and the hotspot amplitude is reduced when aerosols are added to an
535 otherwise clear (Rayleigh scattering only) atmosphere. These results also showed that
536 atmospheric scattering does not generate hotspot-like signatures and does not change the
537 width of the BRDF-induced hotspot.
- 538 4. In VLIDORT, the direct-beam solar reflectance is calculated using the exact BRDF (rather
539 than in a truncated Fourier-series form); this means that smaller values of N_{FOURIER} (i.e. 23
540 and 63 for atmospheres without and with aerosol scattering) can be used in for the multiple
541 scattering calculations in VLIDORT to obtain hotspot signature with acceptable accuracy.

542 Atmospheric corrections in the POLDER data processing were performed using Rayleigh-only
543 single scattering without any consideration of aerosol. Our simulations suggest that the amplitude
544 of hotspot signature at the surface is likely underestimated in the analysis of hotspot signature
545 using POLDER data [Bréon et al., 2002].

546 Another issue related to the hotspot correction in the model used by Lorente et al. [2018] is the
547 scaling by a factor of $3\pi/4$; this may lead to the amplitude of hotspot too high in large solar zenith
548 angle. It is recommended that users take care to check the kernel equations when using the three
549 parameters from MODIS BRDF products to generate the BRDF.

550 Our results highlight the importance of the including aerosol scattering in the retrievals of surface
551 BRDF (hotspot). The agreement between our simulated results and observations from POLDER
552 measurements enhances our understanding of the nature of the hotspot and the impact on it by
553 atmospheric scattering. It is also clear that VLIDORT makes accurate simulations of the hotspot



554 effect, and the results obtained here can be used as benchmarks. Our improved hotspot kernel is
555 now a standard feature in the latest version of the VLIDORT BRDF supplement code.

556

557 **Description of author's responsibilities**

558 XX, XL and RS conceived of the idea. XX and RS led the writing. All authors edited the
559 manuscript.

560 **Funding**

561 This research was supported by NASA SBG program.

562 **CRedit authorship contribution statement**

563 **Xiaozhen Xiong:** Methodology, Writing – original draft, Formal analysis, Investigation. **Xu**
564 **Liu:** Funding acquisition, Supervision, Writing – review & editing, Conceptualization. **Robert**
565 **Spurr:** Methodology, Writing – review & editing, Formal analysis. **Ming Zhao:** Coding,
566 Analysis. **Wan Wu, Qiguang Yang, Liqiao Lei:** Writing – review & editing.

567 **Declaration of Competing Interest**

568 The authors declare that they have no known competing financial interests or personal
569 relationships that could have appeared to influence the work reported in this paper.

570 **Acknowledgements**

571 This research was supported by the NASA SBG program and JPL. Resources supporting
572 this work were provided by the NASA High-End Computing (HEC) Program through the NASA
573 Advanced Supercomputing (NAS) Division at NASA Ames Research Center.
574



575 **References**

- 576 Bacour, C., and F.-M. Bréon. Variability of biome reflectance directional signatures as seen by
577 POLDER, *Remote Sens. Environ.*, **98**(1), 80-95, <https://doi.org/10.1016/j.rse.2005.06.008>, 2005.
- 578 Baldrige, A.M., S. J. Hook; C. I. Grove, and G. Rivera. The ASTER spectral library version 2.0.
579 *Remote Sens. Environ.*, **113**, 711–715, 2000.
- 580 Bicheron, P. and M. Leroy. Bidirectional reflectance distribution function signatures of major
581 biomes observed from space. *Journal of Geophysical Research*, **105**, 26669-26681,
582 <https://doi.org/10.1029/2000JD900380>, 2002.
- 583 Bréon, F.M., F. Maignan, M. Leroy, and I. Grant. Analysis of hotspot directional signatures
584 measured from space. *Journal of Geophysical Research*, **107**, 4282-4296, 2002.
- 585 Chen, J. M., and S. G. Leblanc. A four-scale bidirectional reflectance model based on canopy
586 architecture. *IEEE Transactions on Geoscience and Remote Sensing*, **35**, 1316-1337 (1997).
- 587 Chen, J. M., and J. Cihlar. A hotspot function in a simple bidirectional reflectance model for
588 satellite applications. *Journal of Geophysical Research*, **102**, 25907-25913 (1997).
- 589 de Rooij, W. A., and C. C. A. H. van der Stap. Expansion of Mie scattering matrices in generalized
590 spherical functions. *Astron. Astrophys.*, **131**, 237-248, 1984.
- 591 de Haan, J. F., P. B. Bosma, and J. W. Hovenier. The adding method for multiple scattering of
592 polarized light. *Astron. Astrophys.*, **183**, 371-391, 1987.
- 593 Deschamps, P.Y., F.M. Bréon, M. Leroy, A. Podaire, A. Bricaud, J.C. Buriez, G. Sèze. The
594 POLDER mission: Instrument characteristics and scientific objectives. *IEEE Transactions on*
595 *Geoscience and Remote Sensing*, **32**, 598-615, 1994.
- 596 Egbert, D.D. A practical method for correcting bidirectional reflectance variations. *Proceedings*
597 *of Symposium on Machine Processing of Remotely Sensed Data.*, **1977**, 178-188. Available online:
598 https://docs.lib.purdue.edu/cgi/viewcontent.cgi?article=1204&context=lars_symp (accessed on
599 20/03/2020)
- 600 Gao, B. C., M. J. Montes, C. O. Davis, and A. F. H. Goetz. Atmospheric correction algorithms for
601 hyperspectral remote sensing data of land and ocean. *Remote Sensing Environment*, **113**(S1), S17–
602 S24, 2009.
- 603 Godsalve, C. Bidirectional reflectance sampling by ATSR-2: A combined orbit and scan model,
604 *International Journal of Remote Sensing*, **16**, 269-300, 1995.
- 605 Gutman, G.G. The derivation of vegetation indices from AVHRR data. *International Journal of*
606 *Remote Sensing*, **8**, 1235-1243, 1987.
- 607 Hapke, B.W. Bidirectional reflectance spectroscopy: 1. Theory. *J. Geophys. Res.* **86**, 3039-3054,
608 1981.
- 609 Hapke, B.W. Bidirectional reflectance spectroscopy: 4. The extinction coefficient and the
610 opposition effect. *Icarus* **67**, 264-280, 1981.
- 611 Hess M., P. Koepke and I. Schult, Optical properties of aerosols and clouds: the software package
612 OPAC, *Bull. Am. Meteorol. Soc.*, **79**, 831-844, 10.1175/1520-
613 0477(1998)079<0831:OPOAAC>2.0.CO;2



- 614 Hovenier, J. W., and C. V. M. van der Mee, Fundamental relationships relevant to the transfer of
615 polarized light in a scattering atmosphere. *Astron. Astrophys.*, **128**, 1-16, 1983.
- 616 Jiao, Z., Y. Dong and X. Li, "An approach to improve hotspot effect for the MODIS BRDF/Albedo
617 algorithm," *2013 IEEE International Geoscience and Remote Sensing Symposium - IGARSS*,
618 Melbourne, VIC, Australia, 2013, 3037-3039, doi: 10.1109/IGARSS.2013.6723466.
- 619 Jupp, D. L., and A. H. Strahler, A hotspot model for leaf canopies, *Remote Sens. Environ.*, **38**,
620 193-210, 1991.
- 621 Kimes, D.S. Dynamics of directional reflectance factor distribution for vegetation canopies. *Appl.*
622 *Opt.*, **22**, 1364-1372, 1983.
- 623 Kokaly, R.F.; Clark, R.N.; Swayze, G.A.; Livo, K.E.; Hoefen, T.M.; Pearson, N.C.; Wise, R.A.;
624 Benzal, W.M.; Lowers, H.A.; Driscoll, R.L.; Klein, A.J. USGS Spectral Library Version 7: U.S.
625 Geological Survey Data Series 1035, **2017**, Available online: <https://doi.org/10.3133/ds1035>
626 (accessed on 19/03/2020).
- 627 Kuga, Y., and A. Ishimaru, Retroreflection from a dense distribution of spherical particles, *J. Opt.*
628 *Soc. Am.*, **A1**, 831–835, 1984.
- 629 Kuusk, A., The hotspot effect of a uniform vegetative cover, *Sov. J. Remote Sens.*, **3**, 645-658,
630 1985.
- 631 Lenoble, J., M. Herman, J. Deuzé, B. Lafrance, R. Santer, and D. Tanré. A successive order of
632 scattering code for solving the vector equation of transfer in the earth's atmosphere with aerosols,
633 *J. Quant. Spectrosc. Radiat. Transfer*, **107**, 479–507, <https://doi.org/10.1016/j.jqsrt.2007.03.010>,
634 2007.
- 635 Li, X. W. and A. H. Strahler. Geometric-optical bidirectional reflectance modeling of the discrete
636 crown vegetation canopy: Effect of crown shape and mutual shadowing. *IEEE Trans. Geosci.*
637 *Remote Sens.*, **30**(2), 276–292, 1992.
- 638 Lorente, A., F. Boersma, P. Stammes, G. Tilstra, A. Richter, H. Yu, S. Kharbouche, and J. Muller.
639 The importance of surface reflectance anisotropy for cloud and NO₂ retrievals from GOME-2 and
640 OMI. *Atmos. Meas. Tech.*, **11**, 4509–4529, <https://doi.org/10.5194/amt-11-4509-2018>, 2018.
- 641 Lucht, W., C. B. Schaaf, and A. H. Strahler. An algorithm for the retrieval of albedo from space
642 using semiempirical BRDF models. *IEEE Trans. Geosci. Remote Sens.* **38**, 977-998, 2000.
- 643 Maignan, F., F.-M Bréon, and R Lacaze. Bidirectional reflectance of Earth targets: evaluation of
644 analytical models using a large set of spaceborne measurements with emphasis on the Hotspot,
645 *Remote Sens. Environ.*, **90**(2), 210-220, <https://doi.org/10.1016/j.rse.2003.12.006>, 2004.
- 646 Nicodemus, F.E.; Richmond, J.C.; Hsia, J.J.; Ginsberg, I.W.; Limperis, T. Geometrical
647 considerations and nomenclature for reflectance. U.S. Department of Commerce. **1977**. Available
648 online: [https://www.gpo.gov/fdsys/pkg/GOVPUB-C13-
649 80bc81d1913dfe186083080cbdc8ae75/pdf/GOVPUB-C13-
650 80bc81d1913dfe186083080cbdc8ae75.pdf](https://www.gpo.gov/fdsys/pkg/GOVPUB-C13-80bc81d1913dfe186083080cbdc8ae75/pdf/GOVPUB-C13-80bc81d1913dfe186083080cbdc8ae75.pdf) (accessed on 20/03/2020)
- 651 Pinty, B. and M. Verstraete. Extracting Information on surface properties from bidirectional
652 reflectance measurements. *J. Geophys. Res.*, **96**, 2865-2874, 1991.



- 653 Rahman, H., B. Pinty, and M. Verstraete. Coupled Surface-Atmosphere Reflectance (CSAR)
654 Model: 2. Semiempirical Surface Model Usable With NOAA Advanced Very High Resolution
655 Radiometer Data. *J. Geophys. Res.* **98**, 20791-20801, 1998.
- 656 Ross, J., The radiation regime and architecture of plant stands, Dr. W. Junk Publishers, The Hague,
657 Netherlands (1981).
- 658 Roujean, J.-L., M. Leroy, and P.-Y. Deschamps. A Bidirectional Reflectance Model of the Earth's
659 Surface for the Correction of Remote Sensing Data. *J. Geophys. Res.*, **97**, 20455-20468 (1992).
- 660 Rozanov, V., A. Rozanov, A. Kokhanovsky, and J. Burrows. Radiative transfer through terrestrial
661 atmosphere and ocean: Software package SCIATRAN, *J. Quant. Spectrosc. Radiat. Transfer*,
662 **133**, 13–71, <https://doi.org/10.1016/j.jqsrt.2013.07.004>, 2014.
- 663 Schaaf, C.B., F. Gao, A. H. Strahler, W. Lucht, X. W. Li, T. Tsang, N. C. Strugnell, X. Y. Zhang,
664 Y. F. Jin, J. P. Muller, P. Lewis, M. Barnsley, P. Hobson, M. Disney, G. Roberts, M. Dunderdale,
665 C. Doll, R. P. d'Entremont, B. X. Hu, S. L. Liang, J. L. Privette, and D. Roy. First operational
666 BRDF, Albedo nadir reflectance products from MODIS. *Remote Sens. Environ.*, **83**(1), 135–148,
667 [https://doi.org/10.1016/S0034-4257\(02\)00091-3](https://doi.org/10.1016/S0034-4257(02)00091-3), 2002.
- 668 Schulz, F., K. Stamnes and F. Weng. VDISORT: An improved and generalized discrete ordinate
669 method for polarized (vector) radiative transfer, *J. Quant. Spectrosc. Radiat. Transfer*, **61**, 105-
670 122, 1999.
- 671 Siewert, C. E., On the equation of transfer relevant to the scattering of polarized light. *Astrophysics*
672 *J.*, **245**, 1080-1086, 1981.
- 673 Siewert, C. E., On the phase matrix basic to the scattering of polarized light. *Astron. Astrophys.*,
674 **109**, 195-200, 1982.
- 675 Siewert, C. E., A concise and accurate solution to Chandrasekhar's basic problem in radiative
676 transfer *J. Quant. Spectrosc. Radiat. Transfer*, **64**, 109-130, 2000.
- 677 Siewert, C. E., A discrete-ordinates solution for radiative transfer models that include polarization
678 effects. *J. Quant. Spectrosc. Radiat. Transfer*, **64**, 227-254, 2000.
- 679 Stamnes, K., S.-C. Tsay, W. Wiscombe, and K. Jayaweera, Numerically stable algorithm for
680 discrete ordinate method radiative transfer in multiple scattering and emitting layered media.
681 *Applied Optics*, **27**, 2502-2509, 1988.
- 682 Stamnes, P., J. F. de Haan, and J. W. Hovenier, The polarized internal radiation field of a planetary
683 atmosphere. *Astron. Astrophys.*, **225**, 239-259, 1989.
- 684 Stamnes, K., S-C. Tsay, W. Wiscombe, and I. Laszlo. DISORT: A general purpose Fortran
685 program for discrete-ordinate-method radiative transfer in scattering and emitting media.
686 Documentation Methodology Report, ftp://climate.gsfc.nasa.gov/wiscombe/Multiple_scatt/,
687 [2000](https://doi.org/10.1016/j.jqsrt.2000.07.001).
- 688 Van Roozendaal, M., Y. Wang, T. Wagner, S. Beirle, J.-T. Lin, N. Krotkov, P. Stamnes, P. Wang,
689 H. J. Eskes, and M. Krol. Structural uncertainty in air mass factor calculation for NO₂ and HCHO
690 satellite retrievals, *Atmos. Meas. Tech.*, **10**, 759–782, <https://doi.org/10.5194/amt-10-759-2017>,
691 2017.



- 692 Vermote, E. F., D. Tanré, J. L. Deuzé, M. Herman, and J. J. Morcrette. Second simulation of the
693 satellite signal in the solar spectrum, 6S: an overview. *IEEE Trans. Geosci. Remote Sens.*, **35**, 675–
694 686, 1997.
- 695 Vermote, E., N. Z. El Saleous, and C. O. Justice, Atmospheric correction of MODIS data in the
696 visible to middle infrared: First results. *Remote Sens. Environ.*, **83**(1/2), 97–111, 2002.
- 697 Vermote, E., C. O. Justice and F. -M. Bréon. Towards a Generalized Approach for Correction of
698 the BRDF Effect in MODIS Directional Reflectances. *IEEE Transactions on Geoscience and*
699 *Remote Sensing*, **47**(3), 898-908, doi: 10.1109/TGRS.2008.2005977, 2009.
- 700 Vestrucci, M., and C. E. Siewert, A numerical evaluation of an analytical representation of the
701 components in a Fourier decomposition of the phase matrix for the scattering of polarized light,
702 *JQSRT*, **31**, 177-183, 1984.
- 703 Walthall, C. L.; J. Norman, J. Welles, G. Campbell, and B. Blad. Simple equation to approximate
704 the bidirectional reflectance from vegetative canopies and bare soil surfaces. *Appl. Opt.* **24**, 383-
705 387, (1985).
- 706 Wanner, W.; X. Li, A. H. Strahler. On the derivation of kernels for kernel-driven models of
707 bidirectional reflectance. *J. Geophys. Res.*, **100**, 21077-21089, 1997.
- 708 Wanner, W.; Strahler, A.H.; Hu, B.; Lewis, P.; Muller, J.P.; Li, X.; Schaaf, C.L.B.; Barnsley, M.J.
709 Global retrieval of bidirectional reflectance and albedo over land from EOS MODIS and MISR
710 data: theory and algorithm. *J. Geophys. Res.*, **102**, 17143-17161, 1997.
- 711 Yang, Q., X. Liu, and W. Wu. A Hyperspectral Bidirectional Reflectance Model for Land Surface,
712 *Sensors* **20**(16), 4456; <https://doi.org/10.3390/s20164456>, 2020.
713